Available online at www.sciencedirect.com

ScienceDirect

Proceedings of the Combustion Institute 38 (2021) 2127–2134

Proceedings of the Combustion Institute

www.elsevier.com/locate/proci

Pore-resolved simulations of porous media combustion with conjugate heat transfer

Joseph C. Ferguson [a,*], Sadaf Sobhani [a,b], Matthias Ihme [a]

[a] *Department of Mechanical Engineering, Stanford University, Stanford, CA 94305, United States*
[b] *Sibley School of Mechanical and Aerospace Engineering, Cornell University, Ithaca, NY 14853, United States*

Received 8 November 2019; accepted 7 June 2020
Available online 10 November 2020

Abstract

Porous media combustion (PMC) is an active field of research with a number of potential advantages over free-flame combustors. A key contributor to these phenomena is the interphase heat exchange and heat recirculation from the products upstream to the reactants. In this paper, we present a network model that captures the conjugate heat transfer in pore-resolved 2D simulations of PMC. A series of simulations are presented with varying solid conduction and inlet velocity to isolate the role of conjugate heat transfer on the salient features of the burner, including flame stability, axial temperature profiles, and flame structure. We show that both the flame stabilization and the propagation behavior are strongly related to the conjugate heat transfer, and the flame stability regime is shifted to higher velocities as the conductivity of the solid material is increased.

Keywords: Porous media combustion; Conjugate heat transfer; Pore-resolved simulations

1. Introduction

Porous media combustion (PMC) is a promising combustion technology with a number of potential benefits over free-flame combustion [1], including improved flame stability, lean flammability limit extension, and reduced CO and NO$_x$emissions [2]. PMC enables excess-enthalpy combustion due to the heat recirculation via solid–gas heat exchange [3,4]. In excess-enthalpy (super-adiabatic) combustion, the burned gas temperatures are initially above the adiabatic flame temperature, then decrease as the heat is transferred from the fluid to the inert solid material. This results in a higher local flame speed and an extension of the lean flammability limit [5]. In the filtration combustion literature [6], this combustion regime is referred to as the Low Velocity Regime, where the flame propagation is governed by the thermal interactions between the solid and gas phases.

A challenge in PMC is establishing stable operating conditions. The Peclet number is often used to capture the propagation behavior: $P_e = S_L\bar{d}/\alpha$where $S_L$is the laminar flame speed, $\bar{d}$is the mean pore diameter of the porous medium, and

---

[*] Corresponding author.
E-mail address: joseph.ferguson@stanford.edu (J.C. Ferguson).

https://doi.org/10.1016/j.proci.2020.06.064
1540-7489

$\alpha$is the gas thermal diffusivity. Trimis and Durst [7] proposed a critical Peclet number separating the quenching from the propagation regimes. In their work, a step material was considered, with one material section in each of the two regimes, thus ensuring a stable flame for a range of inflow velocities. A recent alternative design involves continuous gradation of the relevant material morphological properties (i.e. porosity and mean pore diameter), creating a stable flame position that varies with inflow conditions [8].

Volume-averaged models are most-commonly used in simulating PMC [9–11]. Such models offer insights into the overall performance of PMC systems and trade-offs associated with macroscale properties such as overall pressure drop, flame stability regime, and averaged flame profile. Experimental characterization methods include pointwise measurements using thermocouples, exhaust gas analyzers, and pressure transducers [7,12,13].

Although significant advancements have been made to characterize global burner performance, there remain numerous open questions regarding the detailed physical processes and internal flame structure inside the porous media. To address this experimentally, Dunnmon et al. [14] used 3D X-ray computed tomography measurements to examine the pore-scale temperature field, reporting spatial inhomogeneities within the reaction zone and preheating in the upstream section. In addition, pore-resolved simulations can offer key insights into the fundamental behaviors of PMC and can also help to inform volume-averaged models. Sahraoui and Kaviany [15] performed a direct comparison between volume averaged and pore-resolved simulations, showing that the pore-resolved simulations are able to capture the local super-adiabatic behavior in PMC. Bedoya et al. [16] performed numerical simulations with one-step finite-rate chemistry on real geometries of sponge-like structures and found a non-monotonic dependence of the burning velocity on pressure and considerable axial temperature variations. Yakovlev and Zambalov [17] also performed 3D pore-resolved simulations on a packed-sphere bed with radiative conduction.

Sirotkin et al. [18] simulated the PMC process in two-dimensional porous materials using a Smoothed Particle Hydroynamics method at variable equivalence ratios and porosities. Based on their numerical and experimental results, in contrast with continuum model predictions, they showed that there exists a flame-anchored – or stable-flame – regime for a single phase burner. This stability was found to depend on both the equivalence ratio and the porosity. To study the hydrodynamics of flame-structure interactions, numerical simulations of pore-resolved, two-dimensional porous media combustion were conducted where the heat transfer to the solid is neglected to decouple the effects of flame-preheating and flame-topology [19].

In this study, previous model assumptions are extended to include the effects of conjugate heat transfer in order to investigate the fundamental pore-scale behavior of PMC with heat recirculation. Section 2 describes our numerical methods to simulate the gas phase, as well as the heat recirculation using a network-model for conjugate heat transfer. Section 3 presents a series of two-dimensional pore-resolved simulations, with varying solid conduction and inlet velocities, and notable features are discussed. Finally, conclusions and discussions of future work are presented in Section 4.

2. Numerical methods

2.1. *Pore-resolved fluid simulations*

The compressible Navier–Stokes equations are solved using an unstructured finite-volume solver with third order Runge–Kutta time integration. Cantera [20] is used for the finite-rate chemistry in the fluid solver. A 30-species skeletal mechanism by Lu and Law [21], derived from the GRI 3.0 mechanism [22] is used to describe the methane–air chemistry.

One geometry configuration was selected from our past study of pore-scale PMC simulations with adiabatic fluid-structure interfaces, in order to isolate the effects of the conjugate heat transfer from the morphological properties. The geometry, generated in the Porous Microstructure Analysis (PuMA) software [23], is composed of randomly placed non-overlapping cylinders with a diameter of 1.6 mm, a global porosity $\epsilon = 0.7$,and a physical size of $L \times H$where $H = 2$ cmand $L = 4H$. The geometry was discretized using an unstructured triangle mesh with ≈412,000 elements, and an edge resolution of $< 100\,\mu$m, in order to resolve the thermal boundary layer and reaction zones. A grid resolution error estimation is included as supplementary material, where the upper bound of the error was estimated to be <4% for 100 μm vs. 25 μm edge resolutions under the conditions in the presented simulations.

In the presented simulations, symmetric boundary conditions are used for the top and bottom of the simulation domain. A constant mass flow rate boundary condition is used for the inflow, where the pressure and temperature are set to 1 atm and 300 K, and the mass flow rate is modified to control the inflow velocity. At the inflow, the species mass fractions are set to 0.04, 0.2235, and 0.7365 for methane, oxygen, and nitrogen, respectively, resulting in an equivalence ratio of $\phi = 0.714$.

2.2. *Conjugate heat transfer*

To account for conjugate heat exchange between gas-phase and solid matrix, we consider a

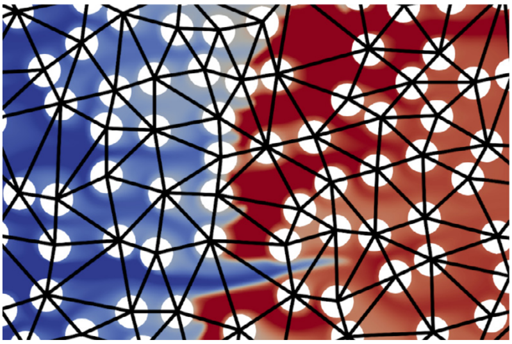

Fig. 1. Visualization of the solid network, constructed with a Delaunay triangulation.

coupling technique similar to that of Sondak and Dorney [24], using the fluid conditions to initialize the solid temperature profile, and time-marching the two solutions via sequential coupling. The coupling between gas-phase and solid matrix requires consideration of boundary conditions. For this, we employ a relaxation algorithm [25] in which the temperature from the solid is imposed on the gas-phase domain, and a Robin-condition is used to couple the heat-flux between gas-phase and solid.

Solid heat transfer is simulated via a network model, similar to that employed by Sahraoui and Kaviany [15], where conductive but fully permeable connections are made between solid elements. Each cylinder is assumed to be at uniform temperature, and heat transfer is modeled between the fluid-solid interface, and between cylinders that are connected in the network. The cylinder connections are assigned via a Delaunay triangulation [26] with between 4 and 6 connections per cylinder. Connections longer than 7.5 mm (which occur at the domain boundaries) are discarded. The local thermal conductivity and cross-sectional areas of the connections determine the effective thermal conductivity for the solid network, while the mass and specific heat capacity of the cylinders govern the thermal capacity. A visualization of the Delaunay triangulation is shown in Fig. 1. The network model is not a precise representation of any given porous media, but rather presents a system to study fundamental effects of heat recirculation on flame structure and propagation.

The local heat conduction equations become:

$$\partial_t Q = -\int_{S_f} \lambda_f \nabla T dS - \int_{S_s} \lambda_s \nabla T dS \qquad (1)$$

where $\partial_t Q$is the total heat transfer rate and $\lambda$is the local thermal conductivity. For this work, $\lambda_f$is taken to be a function of the local temperature, and $\lambda_s$is constant. In discrete form, the flux contributions are summed over each element face and network connection:

$$c_p m d_t T\big|_c = \sum_{f=1}^{N_f} \frac{A_f \lambda_f}{h}(T_f - T_c) + \sum_{s=1}^{N_s} \frac{A_s \lambda_s}{L_s}(T_s - T_c)\,, \qquad (2)$$

where $f$and $s$denote the fluid and solid surfaces, $c$represents the quantities of the solid cylinders, $A$is the connection cross-sectional area, $L_s$is the length of the solid connection, and $h$is the distance from the wall to the fluid cell center. The cross-sectional area and the connectivity of the solid network are both degrees of freedom that can be modified to change the effective thermal conductivity of the solid structure. For the purposes of this study, radiation was neglected and there was no heat loss to the surroundings. One challenge to modeling conjugate heat transfer is the difference in time scale that can exist between the solid and fluid phases. The choice of an initial solid temperature profile becomes important as the time for the solid to equilibrate may be prohibitively long if the initial profile is far from the operating conditions.

In the presented simulations, the flame is initialized by imposing a hyperbolic tangent function for both the temperature and species mass fractions, with the flame at the center of the domain. Based on this fluid temperature profile, the solid temperature is set by solving the steady-state form of Eq. (2), converged via an iterative solver [27]. Once the simulation begins, the solid temperature is modified via explicit Euler time integration of Eq. (2) at a given time-step interval. Given the simplified nature of the network model, the computational expense of the heat transfer is negligible compared to that of the fluid solver.

3. Results and discussion

3.1. Simulatio setup

A series of simulations were performed, in which the solid conductivity and inlet velocity are varied in order to study the effects of the conjugate heat transfer on the transient and steady-state PMC process. The conductivity was divided into an adiabatic case, where there is no heat transfer between the fluid and solid phases, and three cases with varying degrees of solid conductivity. The solid conductivity is parameterized by $\lambda^* = \lambda/\lambda_{Al_2O_3}$,where $\lambda$is the local thermal conductivity assigned to the solid network, and $\lambda_{Al_2O_3}$is the thermal conductivity of alumina, taken here to be 20 W/mK, though this quantity is highly variable based on the specific grade of alumina [28]. The value of λ^*governs the profile of the solid network temperature, thus controlling the amount of heat recirculation in the system. Given the difference in

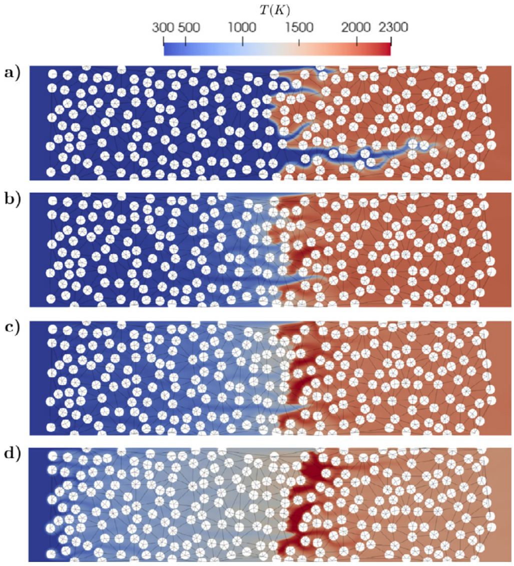

Fig. 2. PMC simulation results at $U_{in}/S_L = 5$ and $C_s^* = 1$ for a) adiabatic fluid-solid boundary conditions, b) λ*= 1, c) λ*= 3, and d) λ*= 10.

the fluid and solid time scales, two sets of simulations were performed: For studying the stability behavior, the thermal capacity, governed by the solid density and specific heat capacity, for the network was chosen to be 5% that of alumina. This allowed for the stability to be studied within the allowable simulation time scales, given the small time step requirement of the gas phase simulations. A second set of simulations was performed in the flash-back regime with the solid density and specific heat capacity equal to that of alumina, to quantitatively study the flash-back behavior. Defining the thermal capacity as $C_s^* = C_s/C_s^{\mathrm{Al_2O_3}}$, we denote these cases as $C_s^* = 0.05$ and $C_s^* = 1$

The second parameter varied in the presented simulations was the inlet velocity, parameterized by the velocity ratio U_{in}/S_L, where S_L is the flame speed of a freely propagating unstretched flame of the same condition. For methane–air combustion at an equivalence ratio of 0.714, the laminar flame speed is 0.2058 m/s, based on the 30 species mechanism [21] used in the presented simulations.

3.2. Simulation results

A simulation snapshot for $U_{in}/S_L = 5$ is shown in Fig. 2 at $t = 0.13$ s. Many of the features associated with porous media combustion can be seen here, including the preheating of the reactants as a function of the solid conductivity. The magnitude of the super-adiabatic combustion is directly related to the amount of preheating, and the level of flame contortion, or the flame length as defined in Section 3.3, is inversely proportional to the magnitude of the preheating.

We seek to define criteria for distinguishing an anchored flame solution from one which propagates through the porous material. We define three steady-state conditions that exist in a quasi-infinite domain: 1) steady flash-back, 2) stable flame and 3) steady blow-off. From the point of view of the solid, we define $\bar{Q}$ as the total thermal energy in the solid. The three configurations are then characterized by $d_t\bar{Q} = \zeta$ where $\zeta > 0$ for steady flash-back, $\zeta = 0$ for a stable flame position, and $\zeta < 0$ for steady blow-off. From the point of view of the flame front, a relevant parameter is the average consumption speed, defined as:

$$S_c = \frac{\int_\Omega \dot{\omega}_F d\Omega}{H \rho_u Y_{F,u}} \tag{3}$$

where $\dot{\omega}_F$ is the rate of fuel mass consumption, and $\rho_u Y_{F,u}$ is the unburned inlet fuel mass density.

In Fig. 3, we present the time-averaged consumption speed as a function of normalized inlet velocity and solid conduction for the parametric study. The error bars indicate one standard deviation, capturing the oscillations and transient behavior in the system. For stable conditions, where the flame is anchored to one point, the consumption speed is equal to the inlet velocity, indicated by the dashed line of unity slope. For a flame flashing back, $S_c > U_{in}$, and for a flame blowing off, $S_c < U_{in}$.

For the case with $\lambda^* = 1$, the simulations show that the critical velocity for flash-back occurs for $3 \leq U_{in}/S_L \leq 4$. For the velocities tested in this study, blow-off only occurs for the case with $\lambda^* = 1$, for which the critical velocity for blow-off occurs between $U_{in}/S_L = 7$ and $U_{in}/S_L = 10$. The results show that the location of the stable flame regime is a function of the solid conductivity, with the adiabatic case showing a stable flame solution at much lower inlet velocities, and the case with $\lambda^* = 3$ having a stable flame regime that is shifted to higher velocities. This shift is explained by the increase in local flame velocity associated with the increased preheating that occurs at higher conductivity values. The case with $\lambda^* = 10$ is neglected from the stability analysis because the physical domain was not large enough to capture a representative solid temperature profile.

Our results indicate, in agreement with the experimental and numerical results presented by Sirotkin et al. [18], that a flame-anchored regime exists for a single phase material, in contrast with predictions from continuum models. However, as expected, this stable zone is quite narrow compared to two-phase or graded configurations.

We proceed by separating our analysis into the transient processes of flash-back and blow-off, and stable flame regime analysis.

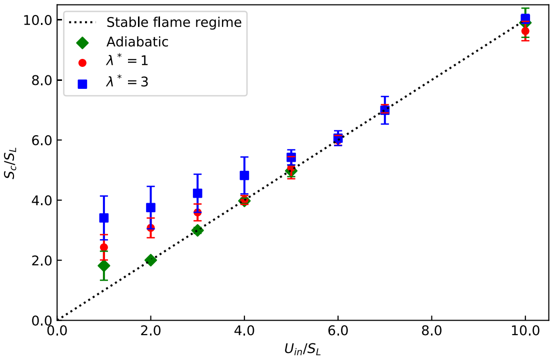

Fig. 3. Consumption speed vs. inlet velocity for the adiabatic, $\lambda^* = 1$,and $\lambda^* = 3$cases at $C_s^* = 0.05$.

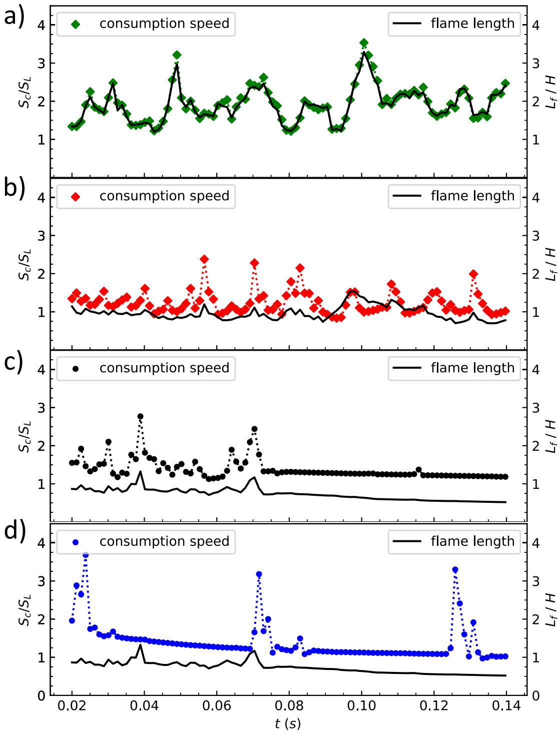

Fig. 4. Transient consumption speed and flame length during flash-back at $U_{in}/S_L = 1$and $C_s^* = 1$for a) adiabatic fluid-solid interfaces, b) λ^*= 1, c) λ^*= 3, and d) λ^*= 10.

3.3. Transient processes

Given the differences in preheating between the cases, we define the flame position based on a reaction progress variable, rather than a temperature isoline. Here we defined the flame length as the length of the isoline at which the mass fraction of methane is 10% of its inlet value, $Y_{CH_4}/Y_{CH_4,0} = 0.1$. The flame length is normalized to the domain height, resulting in a characterization of the flame tortuosity. In Fig. 4, the transient consumption speed and flame length are shown for each of the cases.

In the absence of conjugate heat transfer, referred to as the adiabatic case, flash-back and blow-off is governed by the flame contortion as the flame front passes over the solid obstacles. In this case, the consumption speed is directly proportional to the increased flame length, as seen in Fig. 4. This is analogous to turbulent combustion, for which the

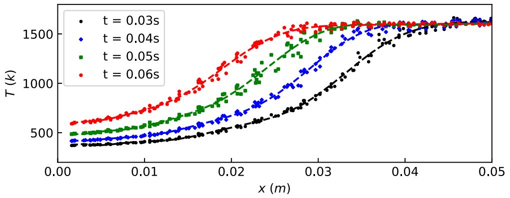

Fig. 5. Evolution of solid phase temperature during flash-back for λ*= 1 and $C_s^* = 0.05$.

turbulent global consumption speed for methane combustion is directly proportional to the flame area [29].

When conjugate heat transfer is introduced, however, flash-back and blow-off are controlled by the evolution of the solid temperature profile. During flash-back, as the flame propagates into a region with colder solid temperature, the flame is quenched as the local flame speed is reduced by the solid heat sink. This can result in an oscillatory flame behavior, also noted by Sirotkin et al. [18], in which the oscillations continue until the local solid temperature rises sufficiently for the flame to continue its propagation. Due to the reactant preheating, the local flame speed is increased, resulting in a reduction in the flame length during the flash-back process, such that $L_f/H < S_c/S_L$.

This transient solid evolution is shown in Fig. 5, where the solid evolution is presented for λ*= 1 and $C_s^* = 0.05$. For a quasi-infinite domain, this temperature profile would continue to be advected at a velocity equal to the flame velocity, characterized by $U_f = S_c - U_{in}$where $U_f < 0$for flash-back and $U_f > 0$ for blow-off.

At high solid conductivity values, a different regime of flash-back can occur, where high levels of preheating result in short bursts of rapid flame propagation with local velocities of up to 4 m/s prior to being quenched by the lower temperature solid. The flame will then remain relatively stationary until the solid temperature has increased sufficiently upstream to trigger another propagation event, as seen in Fig. 4d. One such event is shown in Fig. 6.

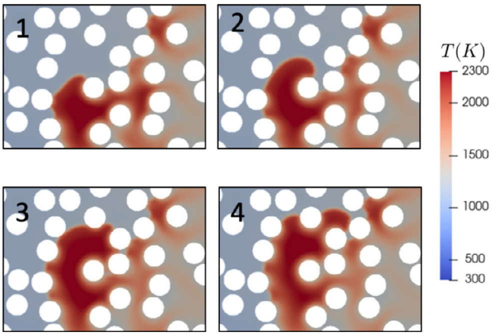

Fig. 6. Visualization of rapid flame propagation front for λ*= 10 and $C_s^* = 1$,with 2.2×10^{-4}s between each frame.

This regime is likely an ignition-assisted propagation mode [30,31], accounting for the high local propagation velocity. The separation between this regime, Fig. 4d, and standard flame propagation, Fig. 4a–c can be seem from the correlation between flame length and consumption speed. For the adiabatic fluid-solid boundary case, the flame length is perfectly matched with the consumption speed, indicating the propagation of a transient, corrugated flame. When conjugate heat transfer is considered, the preheating of the reactants increases the local flame speed, leading to values of L_f/Hthat are below the normalized consumption speed S_c/S_L; however, at lower values of solid conductivity, the flame length is still highly correlated with the consumption speed. As the magnitude of the reactant preheating increases, the flame length becomes more disconnected from the consumption speed. For the case with λ*= 10, these peaks seem to decouple from the local flame length, indicating that the flame corrugation is not the relevant parameter controlling the consumption speed. Rather, flash-back is characterized by a cycle of rapid propagation events, followed by relatively stationary conditions until the nearby solid is sufficiently heated.

During flash-back, the burned gas exiting the domain is at a lower temperature than the adiabatic flame temperature, as some of the heat release of the combustion is deposited into the solid network. The reverse is true in blow-off conditions; since $d_t\bar{Q} < 0$,assuming complete combustion, the exiting burned gas is above the adiabatic flame temperature during a steady blow-off in a quasi-infinite domain. During blow-off, the flame becomes very contorted and the length of the reaction zone increases significantly. The propagation of the blow-off front is mitigated by the ignition of the reactants from the high-temperature solid. As the solid cools, the blow-off front continues downstream.

3.4. Stable flame regime

From Fig. 4, we see that a stable flame exists for each of the three cases shown, and that this stability regime is dependent the solid conduction. To examine the characteristics of the stable-flame regime, 1D projected profiles for the adiabatic, $\lambda^* = 1$,and $\lambda^* = 3$cases are shown in Fig. 7 at $U_{in}/S_L = 7$,a stable flame condition for each of the three cases.

The projected gas temperature is the average gas phase temperature at the specified axial location, which, due to regions of strong flame corrugation, may include regions of burned and unburned mixtures. To provide greater clarity and insight into the superadiabatic flame behavior, the temperatures of the burned and unburned gases are also shown separately. The burned and unburned average temperatures are computed with a method analogous

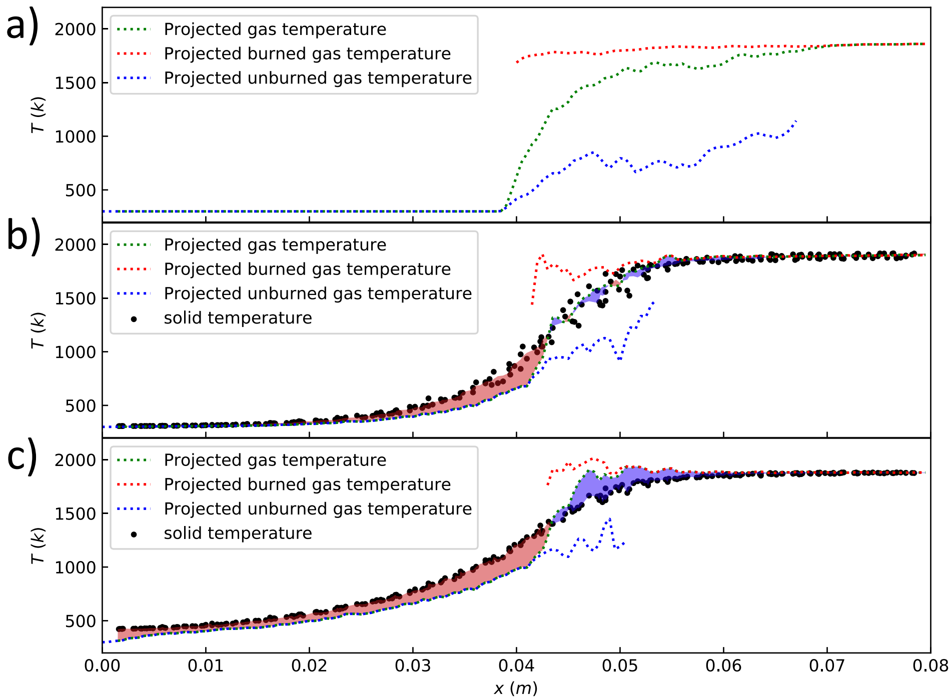

Fig. 7. Projected gas and solid phase temperatures at $C_s^* = 0.05$for a) adiabatic fluid-solid boundaries, b) $\lambda^* = 1$,and c) $\lambda^* = 3$.

to the Bray–Moss–Libby model [32] for turbulent combustion, used to separate the flow into burned and unburned regions. Here, the reaction progress variable is defined as $c = Y_{CH_4}/Y_{CH_4,0}$and the thickness of the flame is assumed to be small compared to the domain length. The integral of the unburned and burned gas temperatures are normalized by their respective probabilities at each axial location, $\alpha(x)$and $\beta(x)$. The unburned and burned projections are shown for $\alpha$and βbetween 0.02 and 0.98. The axial distance for which both unburned and burned projections are shown corresponds to the scale of the flame corrugation. Fig. 7 shows that a higher solid conductivity, and thus more preheating, resulting in a reduction in reaction zone length, due to the higher local flame speed.

In Fig. 7, the region for which $T_f < T_s$is shaded in red, showing the preheat zone. The blue shading indicates regions for which $T_f > T_s$. The overall area of the shaded regions corresponds to the magnitude of the preheating, although any nonlinearities in the thermal properties of both phases must be considered.

4. Conclusions

Simulations of lean-methane porous media combustion are presented, with a solid-network model used to simulate the conjugate heat transfer. From simulations of porous media combustion with an adiabatic solid phase, we find that the contortions of the flame around the porous media results in a relatively large range of stable operating velocities. The introduction of conjugate heat transfer reduces this range of stability by introducing feedback mechanisms for the solid and gas phase temperatures, although a stable regime still exists. For higher values of solid conductivity, in which more preheating occurs, the minimum velocity for a stable flame is found to increase. The flash-back behavior is shown to be strongly dependent on the solid conduction, with a flash-back regime disconnected from the flame corrugation emerging for very high levels of preheating.

Previous studies in porous media combustion have focused primarily on the impact of global burner performance of various burner designs. The results presented in this study aim to enhance the fundamental understanding of porous media combustion by demonstrating key physical mechanisms governing current burner designs, and motivate future designs. In future work, the numerical framework presented in this work can be used to study the internal flame structure effects of two-phase and graded burner designs. Furthermore, the solid network model can be extended to three dimensions to further study effects of geometric complexity on flame behavior.

Declaration of Competing Interest

None.

Acknowledgments

This work is supported by a Leading Edge Aeronautics Research for NASA (LEARN) grant (No. NNX15AE42A) and by the National Science Foundation (Award No. CBET-1800906 and Graduate Research Fellowship with No. 1656518). Resources supporting this work were provided by the NASA High-End Computing (HEC) Program through the NASA Advanced Supercomputing (NAS) Division at Ames Research Center.

Supplementary material

Supplementary material associated with this article can be found, in the online version, at doi:10.1016/j.proci.2020.06.064 .

References

[1] M. Abdul Mujeebu, M.Z. Abdullah, M.Z. Abu Bakar, A.A. Mohamad, R.M.N. Muhad, M.K. Abdullah, *J. Environ. Manage.* 90 (8) (2009) 2287–2312.
[2] S. Wood, A.T. Harris, *Prog. Energy Combust. Sci.* 34 (5) (2008) 667–684.
[3] D.R. Hardesty, F.J. Weinberg, *Combust. Sci. Technol.* 8 (5–6) (1973) 201–214.
[4] J. Buckmaster, T. Takeno, *Combust. Sci. Technol.* 25 (1981) 153–158.
[5] M.H. Akbari, P. Riahi, R. Roohi, *Appl. Energy* 86 (12) (2009) 2635–2643.
[6] V.S. Babkin, *Pure Appl. Chem.* 65 (2) (1993) 335–344.
[7] D. Trimis, F. Durst, *Combust. Sci. Technol.* 121 (1–6) (1996) 153–168.
[8] S. Sobhani, D. Mohaddes, E. Boigne, P. Muhunthan, M. Ihme, *Proc. Combust. Inst.* 37 (4) (2019) 5697–5704.
[9] M. Abdul Mujeebu, M. Zulkifly Abdullah, A.A. Mohamad, M.Z. Abu Bakar, *Prog. Energy Combust. Sci.* 36 (6) (2010) 627–650.
[10] X.Y. Zhou, J.C.F. Pereira, *Fire Mater.* 22 (5) (1998) 187–197.
[11] G. Brenner, K. Pickenacker, O. Pickenacker, D. Trimis, K. Wawrzinek, T. Weber, *Combust. Flame* 123 (1–2) (2000) 201–213.
[12] M.T. Smucker, J.L. Ellzey, *Combust. Sci. Technol.* 176 (8) (2004) 1171–1189.
[13] S. Sobhani, B. Haley, D. Bartz, J. Dunnmon, J. Sullivan, M. Ihme, in: Proceedings of the ASME Turbo Expo 2017: Turbomachinery Technical Conference and Exposition, Volume 5C: Heat Transfer, Turbo Expo: Power Land, Sea, and Air, American Society of Mechanical Engineers Digital Collection, 2017. V05CT17A001
[14] J. Dunnmon, S. Sobhani, M. Wu, R. Fahrig, M. Ihme, *Proc. Combust. Inst.* 36 (3) (2017) 4399–4408.
[15] M. Sahraoui, M. Kaviany, *Int. J. Heat Mass Transf.* 37 (18) (1994) 2817–2834.
[16] C. Bedoya, I. Dinkov, P. Habisreuther, N. Zarzalis, H. Bockhorn, P. Parthasarathy, *Combust. Flame* 162 (10) (2015) 3740–3754.
[17] I. Yakovlev, S. Zambalov, *Combust. Flame* 209 (2019) 74–98.
[18] F. Sirotkin, R. Fursenko, S. Kumar, S. Minaev, *Proc. Combust. Inst.* 36 (3) (2017) 4383–4389.
[19] S. Sobhani, J.C. Ferguson, M. Ihme, Pore-scale Flame Dynamics in Porous Media, 2020, Manuscript in preparation.
[20] D.G. Goodwin, R.L. Speth, H.K. Moffat, B.W. Weber, Cantera: An Object-Oriented Software Toolkit for Chemical Kinetics, Thermodynamics, and Transport Processes, 2018, (https://www.cantera.org) Version 2.4.0. 10.5281/zenodo.1174508
[21] T. Lu, C.K. Law, *Combust. Flame* 154 (4) (2008) 761–774.
[22] G.P. Smith, D.M. Golden, M. Frenklach, N.W. Moriarty, B. Eiteneer, M. Goldenberg, C.T. Bowman, R.K. Hanson, S. Song, W.C. Gardiner, Jr., V.V. Lissianski, Z. Qin, GRI-Mech 3.0, 2000, Available from http://www.me.berkeley.edu/gri-mech/.
[23] J.C. Ferguson, F. Panerai, A. Borner, N.N. Mansour, *SoftwareX* 7 (2018) 81–87.
[24] D.L. Sondak, D.J. Dorney, *J. Propul. Power* 16 (6) (2000) 1141–1148.
[25] M.B. Giles, *Int. J. Numer. Methods Fluids* 25 (4) (1997) 421–436.
[26] D.A. Field, *Commun. Appl. Numer. Methods* 4 (6) (1988) 709–712.
[27] G.L.G. Sleijpen, D.R. Fokkema, *Electron. Trans. Numer. Anal.* 1 (1993) 11–32.
[28] P. Auerkari, Mechanical and Physical Properties of Engineering Alumina Ceramics, *Technical Report*, VTT Technical Research Centre of Finland, 1996.
[29] J.B. Bell, M.S. Day, J.F. Grcar, M.J. Lijewski, *Comm.un App. Math. Comp. Sci.* 1 (1) (2006) 29–51.
[30] K. Grogan, M. Ihme, *Shock Waves* 28 (5) (2018) 941–954.
[31] K.P. Grogan, S.S. Goldsborough, M. Ihme, *Combust. Flame* 162 (8) (2015) 3071–3080.
[32] K.N.C. Bray, P.A. Libby, J.B. Moss, *Combust. Flame* 61 (1) (1985) 87–102.